Article

Gradient-porous-structured Ni-rich layered oxide cathodes with high specific energy and cycle stability for lithium-ion batteries

Zhiyuan Li [1], Yong Wang [1], Jing Wang[2], Changxu Wu[2], Weina Wang[1], Yilin Chen [1], Chenji Hu[1], Kai Mo[3], Tian Gao[3], Yu-Shi He[1], Zhouhong Ren[4], Yixiao Zhang[1,4], Xi Liu [4], Na Liu[2], Liwei Chen [1,4], Kai Wu [2], Chongheng Shen[2] ✉, Zi-Feng Ma[1] & Linsen Li [1,4] ✉

Ni-rich layered oxides ($LiNi_xCo_yMn_{1-x-y}O_2$, $x > 0.8$, NCM) are technologically important cathode (i.e., positive electrode) materials for next-generation high-energy batteries. However, they face challenges in cycle stability and durability due to internal strain accumulation and particle fracture as the batteries cycle. Here we report a simple molten-salt-assisted synthesis route to introduce gradiently distributed pores into the polycrystalline NCM secondary particles. The gradient porous strategy creates void spaces to buffer the anisotropic volume change of the primary particles, effectively mitigating the inter-granular fracture and limiting the impedance growth. It not only increases the maximum accessible capacity of the NCM cathodes but also greatly enhances their cycle stability in practical pouch-type batteries and all-solid-state-batteries. It further enables a high nickel, low cobalt cathode ($LiNi_{0.96}Co_{0.02}Mn_{0.02}O_2$) with a combination of high specific energy (941.2 Wh kg^{-1} based on cathode weight at 0.1 C and 25 °C, 1 C = 245 mA g^{-1}) and high stability during cycling (80.5% capacity retention after 800 cycles at 1 C relative to that of the first cycle) and high-temperature storage (reversible capacity retention >95.5% after 42-day storage at 60 °C at the fully charged state) in pouch cells.

High-energy lithium-ion batteries (> 400 Wh kg^{-1} at the cell level) play a crucial role in the development of long-range electric vehicles and electric aviation[1–3], which demand materials innovations, especially on the cathode (i.e., positive electrode) side. Ni-rich layered oxides ($LiNi_xCo_yMn_{1-x-y}O_2$, $x \geq 0.8$, NCM) have been intensively researched in recent years because of their high specific energy and relatively lower cost compared to the Co-rich cathodes[4–8]. However, the practical application of Ni-rich NCMs is still plagued by complex chemo-mechanical degradations, including surface lattice collapse, oxygen release, cathode-electrolyte side reactions, and transition-metal dissolution, which greatly affect the battery's cycle life and safety[9–11]. These problems are further exacerbated by intergranular fractures induced by electrochemical cycling, which expose fresh internal surfaces susceptible to electrolyte attack and disrupt ion/electron transport within NCM secondary particles (so-called polycrystalline NCM)[12]. The importance of inhibiting NCM particle crack to reduce capacity fade has been widely recognized[13–15].

Crack generation in the polycrystalline NCM is primarily attributed to the non-uniform stress resulting from the anisotropic volume

[1]Department of Chemical Engineering, Shanghai Electrochemical Energy Devices Research Center, School of Chemistry and Chemical Engineering, Shanghai Jiao Tong University, Shanghai, China. [2]Contemporary Amperex Technology Co., Ltd., Ningde, China. [3]Zeiss Shanghai, Shanghai, China. [4]In-Situ Center for Physical Sciences, School of Chemistry and Chemical Engineering, Shanghai Jiao Tong University, Shanghai, China. ✉e-mail: ShenCH@catl.com; linsenli@sjtu.edu.cn

change of the primary particles upon Li extraction/insertion (Fig. 1, left)[16–18]. It was reported that the cracks are preferentially nucleated at the core region of the NCM secondary particles, where there is a greater degree of orientation randomness among the primary crystallites[16,19]. As the battery cycles, the microcracks propagate and merge into larger ones extending from the interior to its surface[20,21]. Making "single-crystal-like" NCM (SC-NCM) particles is a straightforward strategy to reduce such intergranular fracture and greatly enhance the battery cycle stability. This strategy has attracted great research interest recently[22–25]. However, the accessible Li-storage capacity is usually lower for the SC-NCMs compared to their poly-crystalline counterparts with the same chemical composition[26]. Alternatively, the crack generation in the polycrystalline NCMs can be effectively mitigated by grain-boundary modification (for example, by Li_3PO_4[27] and Co_xB[28]), tuning the size, morphology, and orientation of the primary crystallites (mostly by high-valence element doping)[29–32], and concentration gradient design (e.g., Co-rich surface, Ni-rich core)[33]. Although these microstructural engineering strategies have led to remarkable electrochemical performance, they require sophisticated controls over a set of experimental variables, such as the amount of the doping elements, the particle size of the dopant materials, the spatial distribution of the dopant materials after its mixing with the NCM materials or their precursors, and the heating conditions[34,35]. It is also difficult to ensure that the microstructural modifications are uniformly applied in the ensemble of NCM particles (see examples in Supplementary Fig. 1). These challenges motivated us to devise another straightforward strategy to reduce internal strain accumulation, which utilized a simple molten-salt-assisted method to create interconnected internal pores gradient distributed within the NCM secondary particles (Fig. 1, right, GP-NCM).

The structure of the GP-NCM differs from the traditional poly-crystalline NCM, which has a tightly packed primary particle arrangement. The porosity is higher at the core than the exterior, which is designed to suppress the crack nucleation. These pores also provide additional void space to buffer the anisotropic volume change of the primary particles. Hence, the microcracks can be effectively mitigated, alleviating all sorts of surface-related failures. The interparticle contact between the primary particles is also well-preserved during battery cycling, ensuring facile ion and electron conduction. A similar structural design concept was recently demonstrated by Gao et al., who utilized the Kirkendall effect to introduce a central void into the NCM secondary particles to provide buffer space and thus achieve outstanding electrochemical performance[36]. In this work, the as-made GP-NCM exhibits outstanding cycle performance in both liquid-electrolyte-based and all-solid-state batteries (ASSBs). This structural design concept is also applied to a high Ni, low Co cathode ($LiNi_{0.96}Co_{0.02}Mn_{0.02}O_2$) to realize a combination of high specific energy (~ 941 Wh kg^{-1} based on cathode weight) and cycle stability in pouch-type cells.

Results and discussion
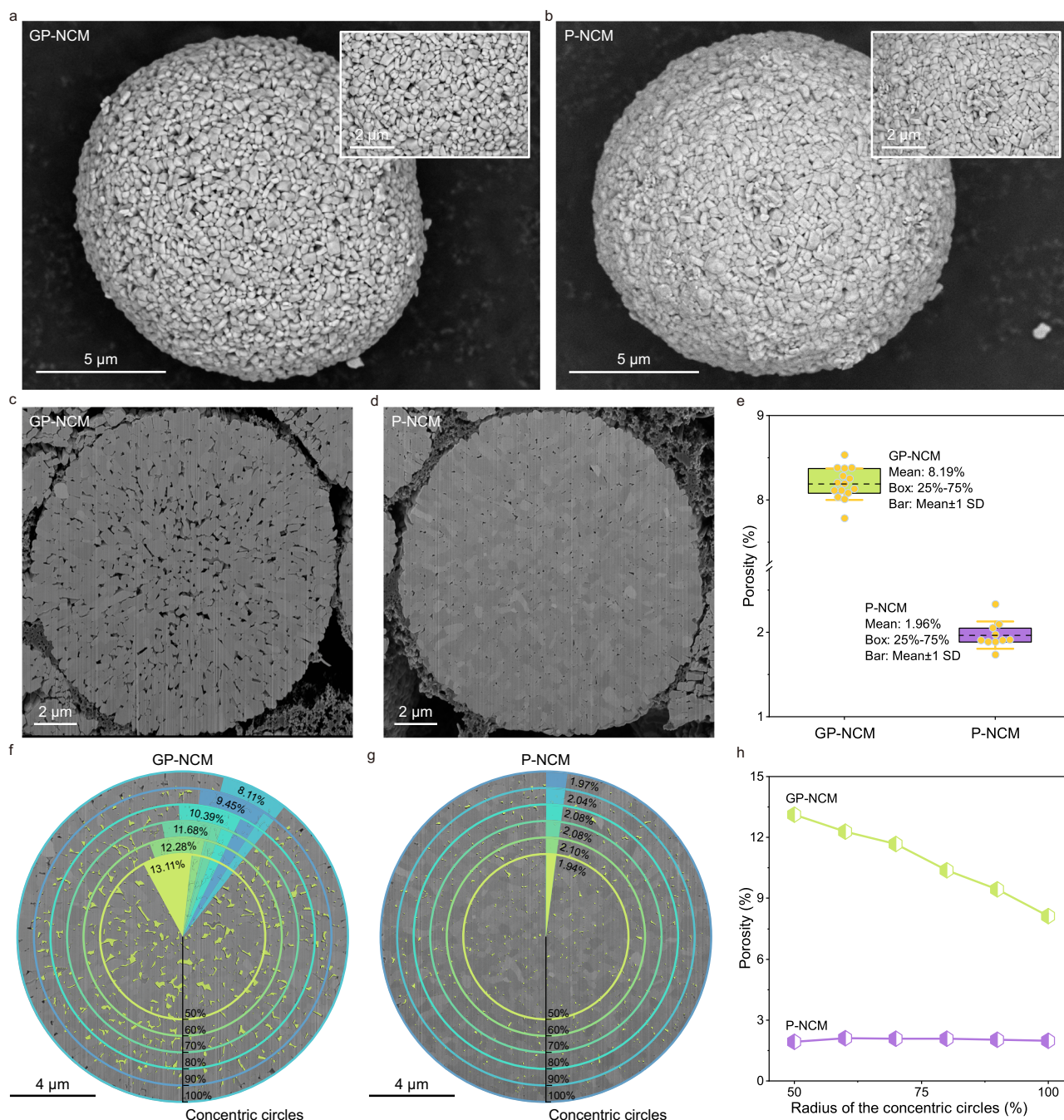### Synthesis and characterizations of GP-NCM

We first demonstrate the GP strategy using a Ni-rich layered oxide cathode ($LiNi_{0.83}Co_{0.11}Mn_{0.06}O_2$) as the model system. The GP-NCM was prepared by introducing a small amount of potassium sulfate (K_2SO_4) into the typical synthesis of NCM, which is a reaction between $Ni_{0.83}Co_{0.11}Mn_{0.06}(OH)_2$ and $LiOH·H_2O$ at high temperature (see Experimental Methods for additional details). K_2SO_4 and LiOH (i.e., the Li source) form a molten-salt mixture upon heating (Supplementary Fig. 2), The molten-salt mixture could infuse into the secondary particles of the NCM precursors. As the LiOH phase was consumed by the transformation of the NCM precursors to the NCM product, the K_2SO_4 phase remained between the primary particles (see elemental mapping results in Supplementary Fig. 3) and likely plays a role in regulating their growth. We note that the molten-salt-based syntheses were more commonly used to prepare single-crystal-like NCM materials in previous literature because the ion migration and crystal growth kinetics are enhanced in the molten salts in comparison to the cases in the solid-state reactions[37–39]. In this work, we used a small amount of K_2SO_4 to enable microstructural tuning of the polycrystalline NCM secondary particles. After the synthesis, K_2SO_4 could be removed by cold-water washing after the synthesis (see inductive coupled plasma-optical emission spectroscopy results in Supplementary Table 1 and chemical mapping results in Supplementary Fig. 4). In previous literature, it was reported that K doping can provide a pillaring effect and improve the structural stability of the NCM cathodes. Slightly increased lattice parameters were observed for those K-doped NCM samples[40,41], which were different from the case of our GP-NCM sample
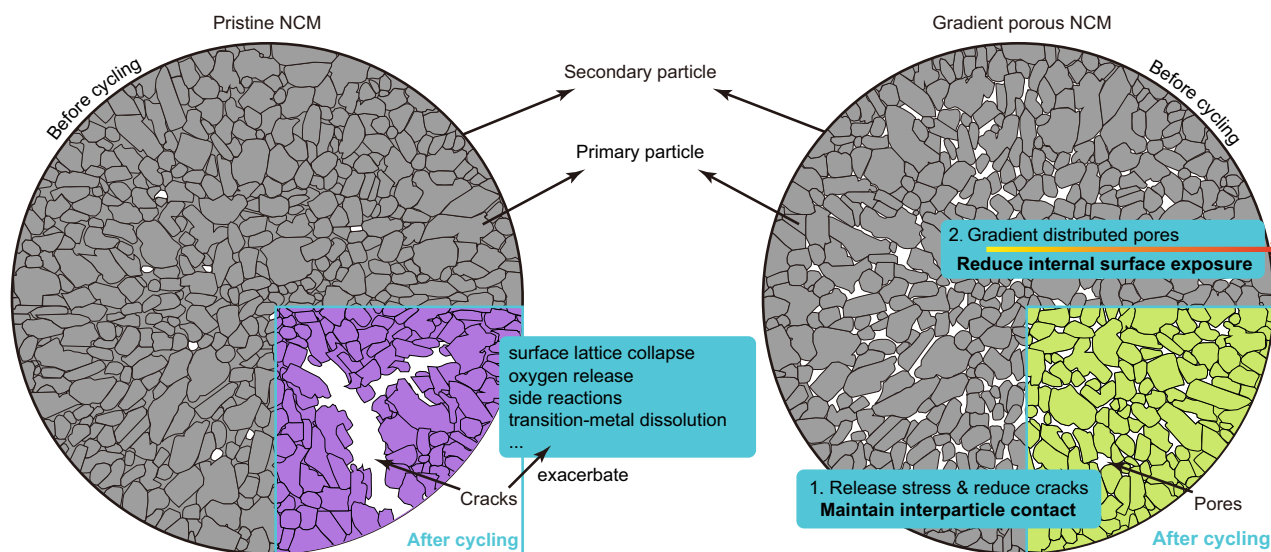
Fig. 1 | The gradient porosity design for NCM cathodes. The cross-sections of the pristine NCM (P-NCM) and the gradient-porous-structured NCM (GP-NCM) before electrochemical cycling are shown as the "Before cycling" areas. There are more voids between the primary particles in GP-NCM compared with P-NCM, in which the primary particles are tightly packed. After cycling, GP-NCM is resistant to intergranular fracture (represented by the bottom right corner region in GP-NCM), whereas severe microcracks occur in P-NCM (represented by the bottom right corner region in P-NCM), exposing internal fresh surfaces to various surface-related degradations. The chemo-mechanical stability of GP-NCM is crucial to its stable cycle performance.

Fig. 2 | Characterizations of GP-NCM. a, **b** are representative SEM images of GP-NCM and P-NCM secondary particles, respectively. High-magnification SEM images are included as the insets, showing a looser primary-particle arrangement in GP-NCM. **c**, **d** are cross-sectional SEM images of GP-NCM and P-NCM, respectively. The cross-sections were prepared by Ar-ion milling. **e** Comparison of cross-sectional porosity of GP-NCM and P-NCM. The porosity was calculated by threshold segmentation based on the grayscale value at each image pixel, with the porous region being darker. The calculation was done for 25 randomly selected cross-sections (15 for GP-NCM versus 10 for P-NCM, see Supplementary Fig. 9 for more details). **f**, **g**, and **h** show the spatial distribution of the internal pores along the radial direction of the secondary particles' cross-sections, which were approximated to a series of concentric circles with different radii, ranging from 50% to 100% relative to the radius of the largest circle.

(see Supplementary Fig. 5 and Supplementary Table 2). For the sake of comparison, we also prepared the pristine NCM (P-NCM) through identical procedures except for the use of K_2SO_4 (see Experimental Methods).

Powder X-ray diffraction and Rietveld refinements confirm that both GP-NCM and P-NCM have highly-ordered layered structures with minimum Li-Ni cation mixings (GP-NCM 1.47% versus P-NCM 1.80%, Supplementary Fig. 5 and Supplementary Table 2). Scanning transmission electron microscopy (STEM) characterizations further

confirmed the highly ordered layered structure (Supplementary Fig. 6). Only a thin cation-mixing layer was observed at the surface of the primary particles. Large field-of-view scanning electron microscopy (SEM) images show that the secondary particles of GP-NCM and P-NCM are highly similar in size and morphology (Supplementary Fig. 7). Two representative high-resolution SEM images of the two samples are shown in Fig. 2a, b. Although the morphology of the primary particles seems indistinguishable, a looser interparticle attachment and some pores could be seen in GP-NCM (see SEM images in

Fig. 2a, b insets), suggesting higher porosity. To provide validations, the secondary particles were polished by argon ion-milling (see Experimental Methods) to allow cross-sectional SEM analysis, which indeed revealed a larger number of internal pores in GP-NCM compared with P-NCM (Fig. 2c, d). Quantitative analysis of the cross-sectional porosity was further performed by threshold segmentation based on the grayscale value at each image pixel[42], with the porous region being darker. The porosity was calculated using the following equation,

$$\text{Porosity} = \left(PC_{pores}/PC_s \right) \times 100\% \tag{1}$$

in which PC_{pores} and PC_s represent the total number of pixels in the pore-containing region and the selected circle area (including as much of the entire secondary particle cross-section as possible), respectively (Supplementary Fig. 8). The calculation was done for 25 randomly selected cross-sections (15 for GP-NCM versus 10 for P-NCM, see Supplementary Fig. 9 for details). The porosity of GP-NCM was consistently higher than P-NCM ($8.19\% \pm 0.19\%$ versus $1.96\% \pm 0.16\%$, Mean ± 1 SD, Fig. 2e). This result was further corroborated by nitrogen physisorption experiments (Supplementary Fig. 10), which revealed that GP-NCM has higher surface area, pore volume, and average pore size than P-NCM (Supplementary Table 3 and Supplementary Fig. 10). The higher porosity of GP-NCM led to a smaller tap density in comparison to P-NCM (1.75 ± 0.03 and 2.17 ± 0.06 g cm^{-3}, Mean ± 1 SD, three measurements in parallel), which brings some challenges in achieving high volumetric energy density. This issue may be mitigated by tuning the internal porosity and/or optimizing the (secondary) particle size distribution (i.e., using large + small particles).

We further analyzed the spatial distribution of the pores along the radial direction in GP-NCM and P-NCM (Fig. 2f, g). The cross-sections of the secondary particles were approximated as a series of concentric circles with different radii, ranging from 50% to 100% relative to the radius of the largest circle. The porosity was calculated using the same threshold segmentation method mentioned above, and the results are summarized in Fig. 2h. GP-NCM exhibits a gradient decreasing porosity from the center (13.11%) to the exterior (8.11%), whereas the pores in P-NCM are uniformly distributed.

Three-dimensional characterization of the internal pore structure in GP-NCM

To better understand the spatial distribution of the internal pores and their interconnection, three-dimensional (3D) tomographic imaging was carried out using a cryogenic focused-ion-beam SEM (FIB-SEM). Figure 3a shows the working principle of the FIB-SEM experiments[43] and the 3D image reconstruction process. A series of SEM micrographs were first recorded at different etching depths with a fixed step size of 20 nm (Fig. 3a1). Then these two-dimensional images were aligned and reconstructed using the Dragonfly software to provide a 3D visualization of the GP-NCM secondary particle (Fig. 3a2). Finally, we applied the grayscale-threshold segmentation method to distinguish between the pores and the solid particles. Figure 3b shows the spatial distribution of the coral-reef-shaped pores with a pore volume larger than 0.002 μm³ (pores smaller than 0.002 μm³ are considered noise pores), using different colors to differentiate the non-connected pores. The statistical analysis of the pore volume is summarized in Fig. 3c. Small pores significantly outnumber the large ones. Approximately 80% of the pores have a pore volume in the range of 0.002 μm³ to 0.010 μm³. Another 16% of them have a pore volume in the range of 0.010 μm³ to 0.030 μm³. Large pores (pore volume > 0.030 μm³) constitute only ~ 4% of the group. By eliminating the small pores (pore volume < 0.030 μm³) shown in Fig. 3b, the spatial distribution of the large pores (pore volume > 0.030 μm³) can be obtained and shown in Fig. 3d. The comparison between the two 3D reconstructions reveals that there are more small pores near the surface of the secondary

particle whereas the large pores are mainly located at the interior. The two largest ones (pore volume: 3.779 μm³ and 1.123 μm³) are located at the center of the secondary particle (Fig. 3d, represented by the orange and blue meshes). These results further confirm that gradient-distributed internal porosity was successfully introduced into the GP-NCM particles.

Electrochemical performance of GP-NCM

The electrochemical performance of GP-NCM was first evaluated in coin-type half cells using Li metal foil as the counter electrode in the voltage range of 4.3 to 2.8 V. GP-NCM exhibited a discharge capacity of 213.3 mAh g^{-1} and a Coulombic efficiency (CE) of 94.8% at the first charge-discharge cycle at 0.1 C (Fig. 4a, 1C = 190 mA g^{-1}), which are evidently higher than those of the control sample (P-NCM, 201.0 mAh g^{-1} and CE = 91.9%). We attribute these improvements to the porous structure, which allows better electrolyte wetting and increases the active surface area. In the cycling test at 1 C-1 C rate, GP-NCM showed remarkable cycle stability by retaining 86.1% of its initial capacity after 300 cycles (Fig. 4b, see the corresponding voltage profiles in Supplementary Fig. 11). P-NCM, by contrast, had a capacity retention rate of 70.6% after 300 cycles. Differential capacity (dQ/dV) analysis was further carried out for both samples, revealing significant peak shifts and increased polarization for P-NCM compared with GP-NCM as the cycle number increased (Fig. 4c, d). GP-NCM also exhibits better rate capability than P-NCM (Fig. 4e). GP-NCM delivered a discharge capacity of 176.6 mAh g^{-1} at 5 C, which is 85.8% of that at 0.2 C (versus P-NCM, 170.0 mAh g^{-1} and 83.8%). The electrochemical performance of GP-NCM is also benchmarked against literature data for Ni-rich NCMs (with similar Ni contents) in terms of the maximum available capacity at 0.1 C and capacity retention rate after 100 cycles at 1 C (Fig. 4f, see more details in Supplementary Table 4), which highlights the benefits of the GP structural design in achieving high specific capacity and outstanding cycle stability simultaneously. We further assembled multi-layered pouch-type full cells[44] (150 mAh in capacity) to evaluate the long-term cycle performance of GP-NCM in the voltage range of 4.2 to 2.75 V at 25 °C, using artificial graphite as the anode (Fig. 4g, N/P ratio ~ 1.1). The pouch cell with the GP-NCM cathode exhibited a cycle life approaching 1000 cycles (78.8% capacity retained), whereas the P-NCM-containing pouch cell lost about half of its initial capacity after 500 cycles.

In addition, GP-NCM also exhibited moderately improved thermal stability in the differential scanning calorimetry (DSC) tests compared with P-NCM (Supplementary Fig. 12), which may also be linked to enhanced mechanical stability. We collected cross-sectional SEM images from the fully charged GP-NCM and P-NCM cathodes (Supplementary Fig. 13). The P-NCM particles already showed some major cracks penetrating the whole particles after the 1st charge process (which was hardly observed in the GP-NCM sample). The more severe cracking led to a higher surface area for the P-NCM sample, which might contribute to a more intense oxygen release and stronger side reactions with the liquid electrolyte during the DSC tests.

GP design preserves solid-solid contact and reduces impedance growth

To understand the performance enhancement brought by the GP structural design, hybrid power pulse characterization (HPPC) tests were first carried out to measure the discharge resistance of GP-NCM and P-NCM. The HPPC test was first proposed by the US Department of Energy as a standardized test to determine the dynamic power capability of a cell over its usable charge and voltage range. Full cells containing GP-NCM or P-NCM were assembled using artificial graphite as the anode and cycled at 1 C (1 C = 190 mA g^{-1}). The HPPC tests were performed after the 1st and the 50th cycles. The testing methodology is based on ref. 45. and illustrated in Supplementary Fig. 14a, b. The discharge resistance was calculated by Eq. 2 based on Ohm's Law, in
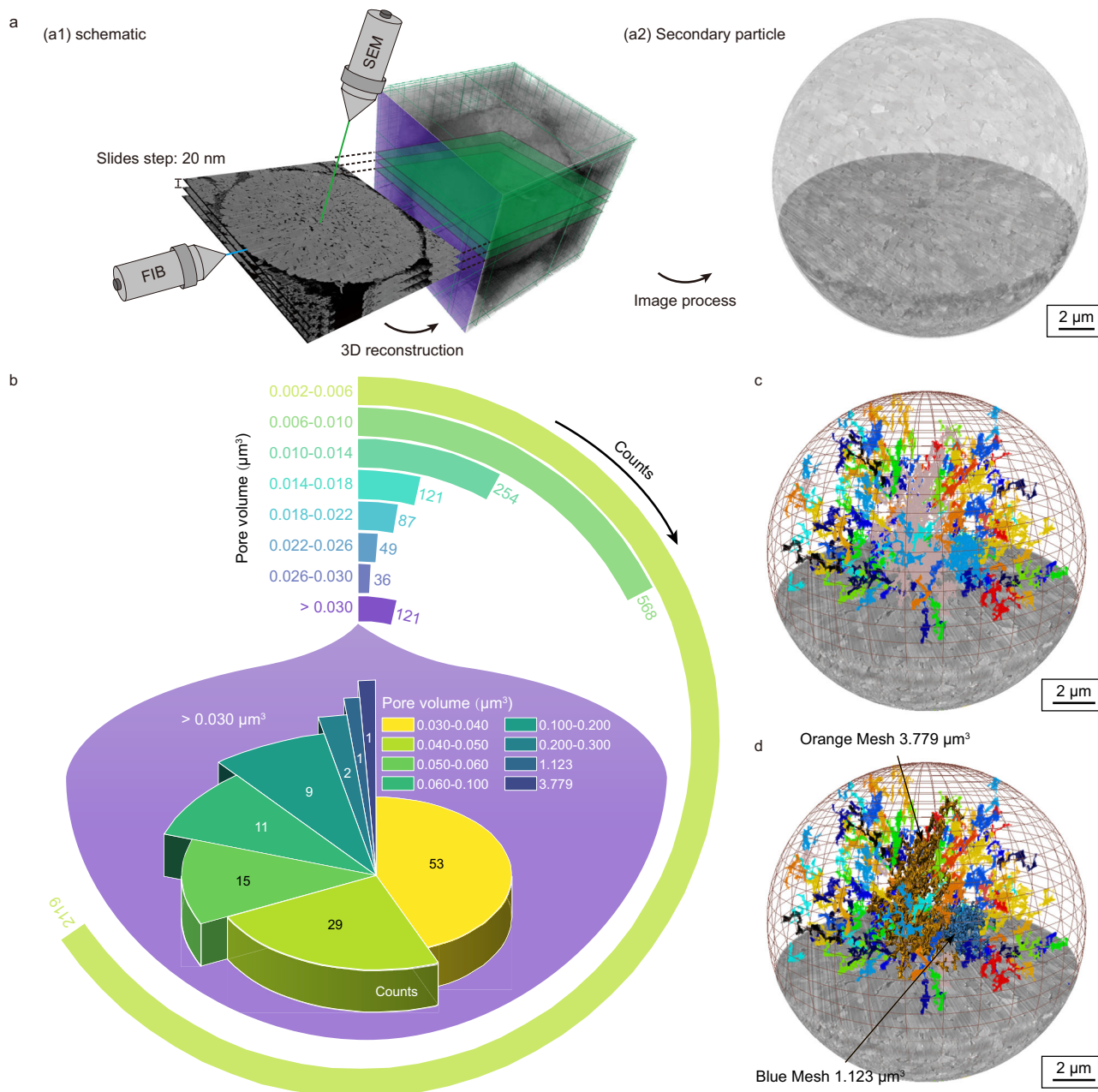
Fig. 3 | Three-dimensional characterizations of the pores in GP-NCM.
a Schematic illustration of the 3D tomographic imaging experiments. Panel (a1) shows that SEM images are continuously acquired as the secondary particle is gradually milled by a focused-ion beam. The SEMs images are aligned and reconstructed to provide a 3D visualization of the secondary particle (a2). **b** Pore analysis derived from the 3D reconstruction results. **c** The pore volume distribution inside the GP-NCM secondary particle. The sector diagram inside the purple area specifies the pores with pore volume > 0.030 μm^3. **d** The 3D spatial distribution of large pores (pore volume > 0.030 μm^3). This 3D reconstruction was made by eliminating the small pores (pore volume < 0.030 μm^3) shown in Panel (**b**), which proves that large pores are mainly located at the interior of the secondary particle.

which V_{t0} and V_{t1} correspond to the voltages at time t_0 and t_1, respectively, while I_{dis} is the discharge current. The resistance data were further used to calculate the pulse power capability by Eq. 3.

$$R_{discharge} = \left| \frac{V_{t1} - V_{t0}}{I_{dis}} \right| \qquad (2)$$

$$Power\ Capability = V_{t1} \times (V_{t0} - V_{t1})/R_{discharge} \qquad (3)$$

Figure 5a summarizes the discharge impedances of GP-NCM and P-NCM at a series of state-of-charge (SoC) after the 1st and 50th cycles. GP-NCM exhibits a smaller increase in discharge resistance compared

to P-NCM, especially at the beginning and near the end of the discharge. In addition, GP-NCM always provided higher power output than P-NCM (Supplementary Fig. 14c, d). The electrochemical impedance spectroscopy (EIS) measurements and the fitting results also revealed smaller changes in cell impedance after cycling, especially in the charge-transfer resistance (Fig. 5b, c see more details in Supplementary Table 5). These findings are consistent with the dQ/dV analysis results (Fig. 4c, d) and imply that the electrochemical-cycling-induced structural damages are likely alleviated in GP-NCM.

STEM characterizations were performed to evaluate the structural changes after about 100 cycles at the atomic scale (Fig. 5d, e). Thin specimens from the cracked region of the secondary particles were
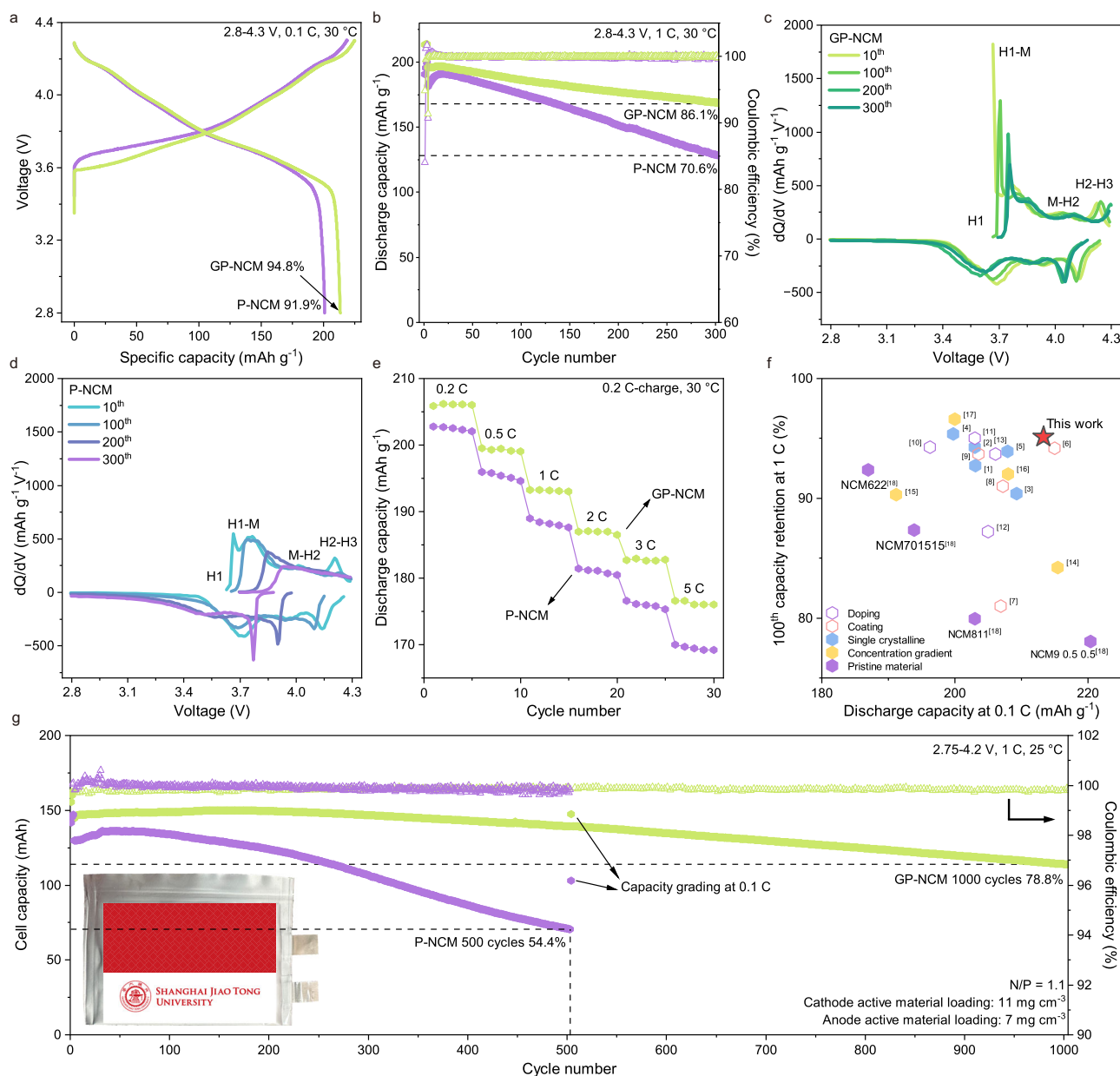
Fig. 4 | Electrochemical performance of GP-NCM. a Voltage profiles of GP-NCM and P-NCM at the first charge-discharge cycle at a C-rate of 0.1 C (1 C = 190 mA g^{-1}) between 2.8 and 4.3 V at 30 °C, which were measured in half cells using Li metal as the counter electrodes. **b** Cycle performance of GP-NCM and P-NCM at 1 C-1 C. A constant-voltage charging step was adopted, and the cut-off C-rate was set at 0.1 C. The capacity retention is calculated based on the 1st cycle of 1 C. **c, d** are differential capacity versus voltage plots (dQ/dV) at the 10th, 100th, 200th, and 300th cycles of GP-NCM and P-NCM, respectively. **e** Rate capability tests of GP-NCM and P-NCM. The cells were first cycled at 0.1 C for five cycles. Then, they were charged at 0.2 C to 4.3 V and discharged to 2.8 V at different C-rates. **f** Comparison of specific capacity at 0.1 C and capacity retention after 100 cycles at 1 C between GP-NCM and Ni-rich NCMs modified by other strategies reported in previous literature. See more details on the reference work in Supplementary Table 4. **g** Cycle performance of GP-NCM and P-NCM in practical pouch-type cells, using artificial graphite as the anode. These full cells were cycled between 2.75 and 4.2 V at 25 °C at 1 C-1 C. These cells were cycled at 0.1 C every 500 cycles, a process called "capacity grading". The cells released higher capacities when the current was reduced, which led to the data spikes. The inset is a photograph of the assembled full cells. The reversible capacity in Fig. 4g is shown in the unit of mAh (the total capacity of the pouch cells), instead of mAh g^{-1} (i.e., the specific capacity of the cathode). The capacity retention is calculated based on the 1st cycle of 1 C.

prepared by FIB (Supplementary Fig. 15), which, in theory, should exhibit the most dramatic structural changes. High-angle annular dark-field (HAADF) imaging revealed the formation of the rock-salt-like (RS) phase (i.e., the cation-mixing phase) at the surface of the primary particles in both GP-NCM and P-NCM samples after cycling whereas the bulk lattice retained the highly ordered layered structure (see Fig. 5d, e, and the corresponding fast-Fourier-transform diffractograms in the insets). Despite the contrast in the capacity retention rate, the thickness of the RS-like surface layer was actually quite comparable

in GP-NCM and P-NCM (~7 nm versus ~9 nm). Therefore, we believe that the performance enhancement in GP-NCM may not be simply attributed to the reduced surface phase transition from the original layered structure to the RS-like structure, although this is often suggested in the literature.

We complemented the atomic-scale characterizations with statistical analysis of the secondary particles' fracture behaviors at the electrode level (i.e., multiple particles). Duplicate GP-NCM and P-NCM cathodes were prepared. They were calendared to a density of
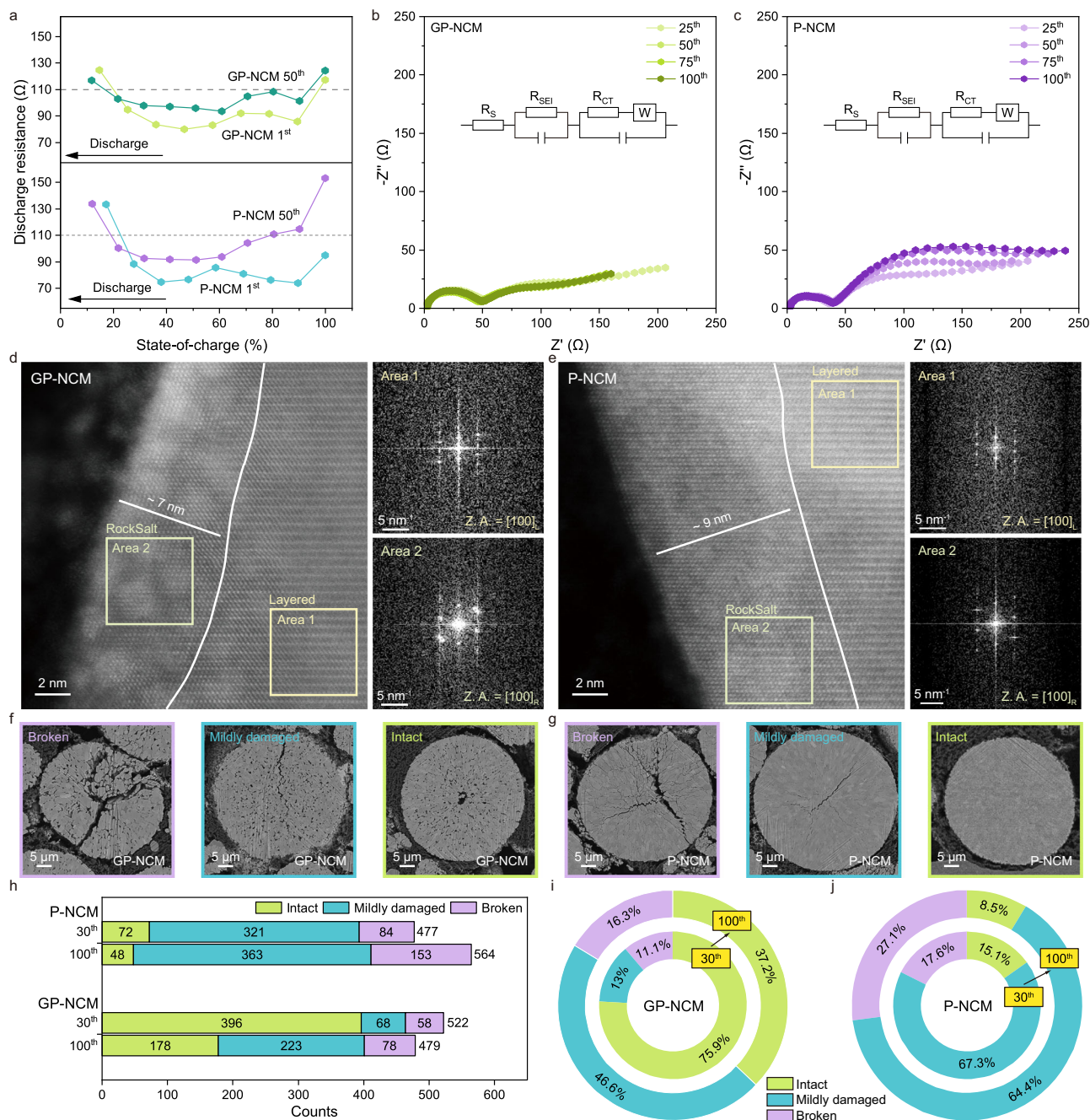
Fig. 5 | Mechanistic studies. a HPPC results of GP-NCM and P-NCM full cells measured at a series of SoCs. These cells were cycled at 1 C-1 C rate. The HPPC tests were carried out after the first and the 50th cycles. **b**, **c** are EIS spectra of GP-NCM and P-NCM half cells measured after the 25th, 50th, 75th, and 100th cycles, respectively. The equivalent circuit model is shown in the inset. **d**, **e** are STEM-HAADF images of primary particles' surface after cycling and the associated fast-Fourier-transform diffractograms. These samples were prepared by FIB and cut from the cracked region of the NCM secondary particles (see Supplementary Fig. 15). **f**, **g** show the representative cross-sectional SEM images of broken, mildly damaged, and intact NCM secondary particles for cycled GP-NCM and P-NCM, respectively. **h** Counts of different types of particles after 30 and 100 cycles at 1 C. The corresponding percentages are shown in panels (**i** and **j**). 2042 secondary particles were analyzed. Their cross-sectional SEM images are included in Supplementary Figs. 16–19.

~ 3.2–3.3 g cm^{-3} using a roller press before the electrochemical measurements. They were cycled at a 1 C rate (1 C = 190 mA g^{-1}) and stopped after 30 and 100 cycles, respectively (capacity retention is shown in Supplementary Table 6). The cross-sections of the cathodes were prepared by argon ion-milling and inspected by SEM, which include 2,042 NCM secondary particles (see images in Supplementary Figs. 16–19). Based on the degree of the particle fracture, the NCM secondary particles were divided into three groups, namely the intact particles, mildly damaged particles, and broken particles (see representative examples in Fig. 5f, g). The statistical analysis results are summarized in Fig. 5h–j. After 30 cycles, 75.9% of the GP-NCM secondary particles remained intact, while 67.3% of the P-NCM secondary particles became mildly damaged, and another 17.6% of them were already broken. Although the particle cracking situations worsened in both samples after 100 cycles, an even sharper contrast was observed. 37.2% of the GP-NCM secondary particles remained intact, in comparison to 8.5% for P-NCM (Fig. 5j). These statistically significant results confirm that the GP structural design effectively
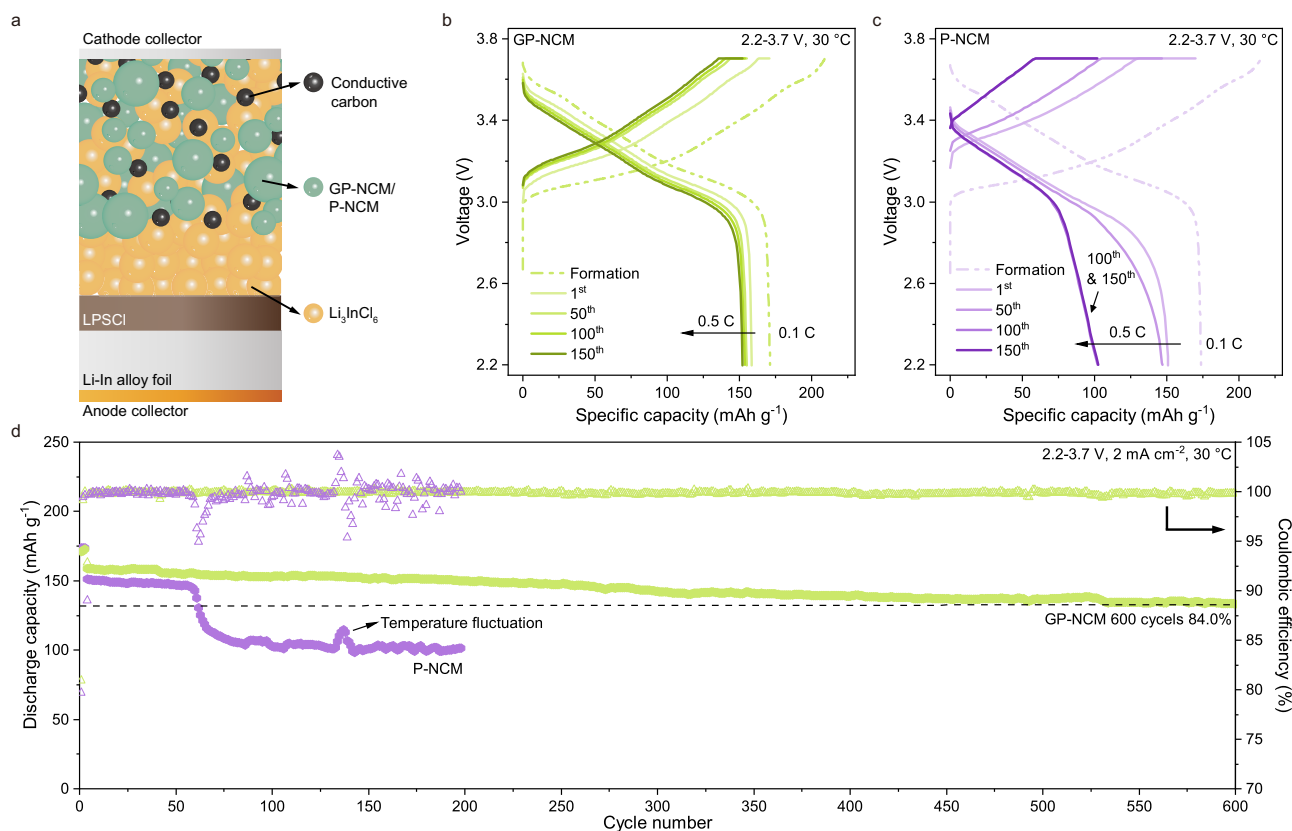
Fig. 6 | GP-NCM as a high-performance ASSB cathode. a Schematic illustration of the ASSB. **b**, **c** are voltage profiles of GP-NCM and P-NCM between 2.2 V and 3.7 V (The potential of anode Li-In reference versus Li⁺/Li is 0.6 V), respectively. The ASSBs were cycled at 0.1 C (1 C is approximately ~ 4 mA cm⁻²) for three cycles and then switched to 0.5 C-0.5 C cycling between 2.2 V and 3.7 V in the subsequent cycles. A constant-voltage charging step was adopted during the 0.5 C cycling, and the cut-off current was approximately 0.05 C. **d** Cycle performance of GP-NCM and P-NCM in ASSBs under a stack pressure of 100 MPa at 0.5 C (2 mA cm⁻²) at 30 °C. The capacity retention is calculated based on 1ˢᵗ cycle of 0.5 C.

suppresses secondary particle fracture, which not only reduces the exposure of fresh internal surfaces to electrolyte attack (relevant to the surface phase transition) but also preserves the solid-solid contact that is crucial to efficient ion and electron conduction within the NCM secondary particles. These synergistic effects slowed down the impedance growth in GP-NCM and contributed to its outstanding electrochemical performance.

**The application of GP-NCM in all-solid-state batteries**

All-solid-state batteries (ASSBs) have gained significant attention recently due to their potential to simultaneously achieve high specific energy density and high safety[46–49]. Maintaining good interfacial contact is a more pressing need in ASSBs because solid-state electrolytes (SSEs) do not "wet" the electroactive particles like the liquid ones. When the electroactive particles are fractured, Li-ion and electron conduction pathways are severely disrupted, thus compromising the electrochemical performance. The outstanding stability of GP-NCM in liquid-electrolyte-based batteries inspired us to explore its application in ASSBs (Fig. 6a). GP-NCM was mixed with a halide-based SSE (Li₃InCl₆)[8] to produce a solid cathode, which is contact with a Li₆PS₅Cl SSE interlayer. Li-In alloy was used as the anode. The GP-NCM solid cathode delivered a similar capacity with P-NCM (171.1 mAh g⁻¹ versus 173.6 mAh g⁻¹, Fig. 6b, c) at 0.1 C (1 C is approximately ~ 4 mA cm⁻²) in the voltage range of 3.7−2.2 V (the potential of anode Li-In reference versus Li⁺/Li is ~ 0.6 V). When they were cycled at a current density of 2 mA cm⁻² (approximately 0.5 C rate), the GP-NCM solid cathode retained 84.0% of its initial capacity after 600 cycles, whereas the P-NCM solid cathode exhibited a sharp capacity decay after only 55

cycles and then slowly degraded afterward (Fig. 6d). These results demonstrate the strength of GP design for the ASSB cathodes.

GP-NCM with a high Ni content and specific energy

We further applied the GP structural design to a high Ni, low Co cathode (LiNi₀.₉₆Co₀.₀₂Mn₀.₀₂O₂, GP-Ni96) and were now able to perform the synthesis at the pilot-scale (~ 100 kg/batch). Figure 7a shows the cross-section of a GP-Ni96 secondary particle, in which a large number of internal pores can be observed. This microstructure differs greatly from that of the control sample (P-Ni96), in which the primary particles are more tightly packed (Fig. 7b). The porosity of GP-Ni96 was measured at 6.92% using the same method aforementioned, while P-Ni96 showed a porosity of 2.25%. In the electrochemical tests, GP-Ni96 delivered a high discharge capacity of 245.8 mAh g⁻¹ and CE of 97.7% (~ 0.89 Li⁺ per structural unit was extracted) during the first charge-discharge cycle at 0.1 C and 25 °C (Fig. 7c, 1 C = 245 mA g⁻¹), clearly outperforming the control sample (239.9 mAh g⁻¹ and 94.7%). This translates to high specific energy of 941.2 Wh kg⁻¹ based on cathode weight at 0.1 C, 888.8 Wh kg⁻¹ at 0.33 C, and 854.1 Wh kg⁻¹ at 0.5 C for GP-Ni96 (Fig. 7d), which is a great upgrade over the existing Ni-rich or Co-based layered oxide cathodes (< 850 Wh kg⁻¹ at 0.1 C according to ref. [1]). Remarkably, the cycling stability was not compromised for GP-Ni96 despite its high Ni content. Pouch-type full batteries containing the GP-Ni96 cathode (with an electrode press density of 3.4 g cm⁻³) exhibited stable cycling over 800 cycles at 1 C-1 C rate, in stark contrast to 280 cycles for P-Ni96 (Fig. 7e). In the high-temperature storage tests at 60 °C[50], the fully charged GP-Ni96-containing batteries also exhibited very good performance (inset in
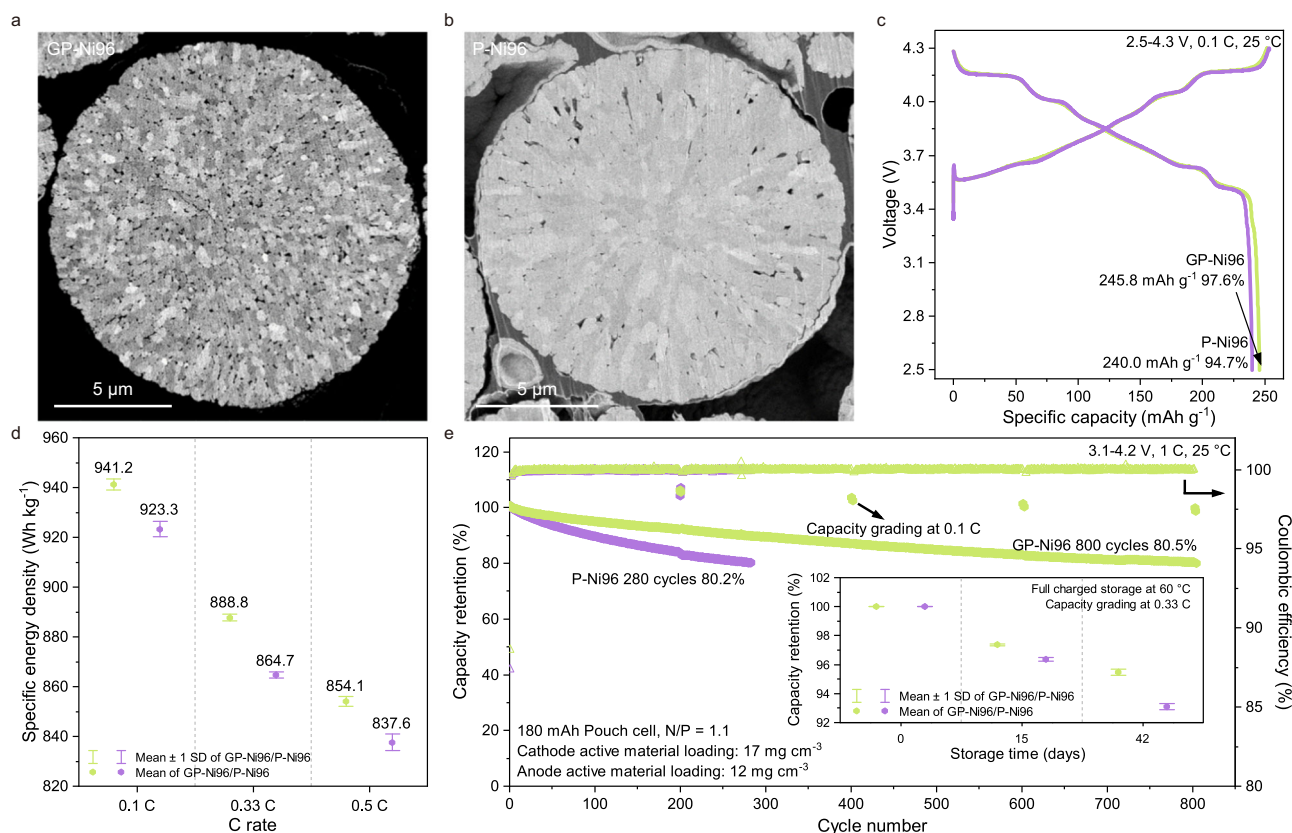
Fig. 7 | GP-NCM with a high Ni content and specific energy. a, b are cross-sectional SEM images of GP-Ni96 ($LiNi_{0.96}Co_{0.02}Mn_{0.02}O_2$) and P-Ni96, respectively. **c** Voltage profiles of GP-Ni96 and P-Ni96 at the 1st charge-discharge cycle at 0.1 C (1 C = 245 mA g^{-1}) and 25 °C, which were measured in half cells using Li metal as the counter electrodes. **d** Specific energy density based on the cathode of GP-Ni96 and P-Ni96 cathodes at 0.1 C, 0.33 C, and 0.5 C, respectively. In each group, four batteries were tested. **e** Cycle performance of GP-Ni96 and P-Ni96 in practical pouch-type full cells at 1 C rate and 25 °C, using artificial graphite as the anode. The full cells were cycled between 3.1 and 4.2 V. Capacity grading was carried out at 0.1 C every 200 cycles. The capacity retention is calculated based on the 1st cycle of 1 C. The inset shows the results from high-temperature storage tests. Three duplicate pouch cells for each group were fully charged to 4.2 V and stored in a constant-temperature chamber set at 60 °C. The reversible capacity after storage was measured by cycling the batteries at 0.33 C between 3.1 and 4.2 V (after 15 and 42-day storage).

Fig. 7e). After 42-day storage, the reversible capacity retention rate was 95.5% ± 0.2% (versus 93.1% ± 0.2% for P-Ni96, mean ± 1 SD). We also note that such performance was achieved without additional doping, surface coating, or electrolyte engineering, which demonstrates the effectiveness of the GP structural design for the high Ni cathodes and suggests that further improvements are optimistic.

Conclusions

In this work, we have demonstrated a simple method to introduce gradient porosity into Ni-rich NCM secondary particles to reduce the electrochemically induced internal strain accumulation. The spatial distribution and interconnectivity of the internal pores were systematically characterized by cross-sectional SEM and FIB-tomographic imaging. GP-NCM offered higher specific capacity, better rate capability and thermal stability, and outstanding cycle performance in practical pouch-type full cells (~79% capacity retention after 1000 cycles) compared with the conventional NCM. Mechanistic studies performed on more than 2000 secondary particles reveal that the GP design effectively mitigates intergranular fracture. As a result, it reduces the exposure of internal fresh surfaces to electrolyte attack and preserves the solid-solid contact that is crucial to control the impedance growth. With the enhanced chemo-mechanical stability, GP-NCM also showed remarkable cycle stability in the next-generation ASSBs. Finally, we extended the GP design to a high Ni, low Co cathode ($LiNi_{0.96}Co_{0.02}Mn_{0.02}O_2$) and demonstrated a combination of high specific energy (941.2 Wh kg^{-1} based on cathode weight) and stable cycle performance (~80% after 800 cycles in pouch cells). This work opens innovative design space for many electrodes used in advanced batteries.

Methods
Materials synthesis
Battery-grade $Ni_{0.83}Co_{0.11}Mn_{0.06}(OH)_2$ hydroxide precursor was acquired from the China Guizhou Zoomwe group. GP-NCM ($LiNi_{0.83}Co_{0.11}Mn_{0.06}O_2$) was synthesized by mixing the hydroxide precursor, $LiOH·H_2O$ (99%, Adamas), and K_2SO_4 (99%, Greagent) in a mole ratio of 1:1.05:0.1, followed by heating the mixture at a heating rate of 5 °C min^{-1} to 760 °C in a tube furnace under flowing high-purity oxygen. The temperature of the tube furnace was held at 760 °C for 12 h before it was cooled to 300 °C at a cooling rate of 2 °C min^{-1}. Then, it was allowed to cool down naturally. The reaction product was washed with cold deionized water twice and ethanol (95%, Greagent) once to remove K_2SO_4. After that, the powders were dried at 80 °C for 5 h and thermally treated again at 650 °C for 10 h under flowing oxygen. P-NCM ($LiNi_{0.83}Co_{0.11}Mn_{0.06}O_2$) was synthesized the same way as GP-NCM except for the addition of K_2SO_4.

GP-Ni96 ($LiNi_{0.96}Co_{0.02}Mn_{0.02}O_2$) was synthesized from the $Ni_{0.96}Co_{0.02}Mn_{0.02}(OH)_2$ hydroxide precursor via the same way as that is described above for GP-NCM ($LiNi_{0.83}Co_{0.11}Mn_{0.06}O_2$), but at a lower synthesis temperature of 700 °C because of its higher Ni content. P-Ni96 ($LiNi_{0.96}Co_{0.02}Mn_{0.02}O_2$) was synthesized the same way as GP-Ni96 except for the addition of K_2SO_4. All samples were stored in hot-sealed vacuum pouch bags before they were used for characterization or electrochemical measurements.

Material characterizations

The crystalline structure of P-NCM and GP-NCM were examined by powder XRD using an X-ray diffractometer (Bruker D8 ADVANCE Da Vinci, with Cu Kα radiation). The chemical composition of the cathode materials was confirmed using ICP-OES (iCAP™ 7600, Thermo Fisher). Particle cross-sections were obtained by Ion-million using an ion beam slope cutter (Leica EM TIC 3X), the samples were carried out at 7.0 V for 1.5 h and 5.0 V for 10 min. The surface morphology of materials and electrodes was explored by SEM (Navigator-100, FBT; Gemini 300, Zeiss; Apreo 2S, Thermo Fisher). The element distribution mapping was explored by SEM-EDS (RISE-MAGNA, Tescan). Porosity was measured using the Surface Area & Porosimetry System (ASAP2460, Micromeritics) based on the Brunauer-Emmett-Teller theory. DSC results were obtained by NETZSCH DSC (204 F1 Phoenix). The sample consists of 5 mg powder (at the fully charged state) and 2 mg liquid electrolyte, and it is heated at a rate of 10 °C min^{-1} from room temperature to 400 °C. Internal pore structures were characterized by FIB-SEM using ZEISS Crossbeam 550, followed by 3D reconstruction using image processing in the Dragonfly software. STEM was carried out by Hitachi HF5000 at an acceleration voltage of 200 kV.

Electrochemical measurements

The cathodes were prepared by mixing active materials, Super-P carbon black and poly(vinylidene) fluoride (PVDF) in N-methyl-2-pyrolidone (NMP) solvent with a mass ratio of 90:5:5. The solid content of the slurry was adjusted to ~ 50% by adding additional NMP. The slurry was evenly coated onto aluminum foil (99.99%, thickness of 13 μm), dried at 80 °C for 2 h, and then at 120 °C under vacuum overnight. The active materials loading of the cathodes used in the coin-type half-cells (CR2025) was between 6 and 8 mg cm^{-2}. The half-cells were assembled using Li foil (99.9%, diameter of 10 mm, thickness of 1 mm, China Energy Lithium Co., Ltd.) as the anode, a polyethylene separator (thickness of 16 μm, Celgard), and a liquid electrolyte (200 μL) consisting of 1.2 M LiPF$_6$ dissolved in ethylene carbonate-ethyl methyl carbonate (30:70 by weight) with 2 wt.% vinylene carbonate additives. The half-cells of GP-NCM and P-NCM (LiNi$_{0.83}$Co$_{0.11}$Mn$_{0.06}$O$_2$) were first cycled at 0.1 C three times, followed by cycling at 1 C-1 C (1 C = 190 mA g^{-1}). The C-rate of half-cells of GP-Ni96 and P-Ni96 (LiNi$_{0.96}$Co$_{0.02}$Mn$_{0.02}$O$_2$) are the same, except for 1 C = 245 mA g^{-1}. The cells were charged in a constant-current/constant voltage mode (CC-CV). The cut-off C-rate for the CV charging step was set at 0.1 C. In the rate capability test, the half-cells were cycled at 0.1 C five times, followed by charging at 0.2 C and discharging at 0.2, 0.5, 1, 2, 3, and 5 C. EIS measurements were conducted on duplicate cells discharged to 2.7 V (versus Li/Li$^+$) after 25, 50, 75, and 100 cycles.

The pouch cells were assembled using artificial graphite (MCMB, BTR) as the anode (single coated, 21.09 cm^2, the corresponding cathode area is 19.25 cm^2). The ratio of negative to positive electrode capacity (N/P ratio) was adjusted to ~ 1.1. For GP-NCM and P-NCM, the cathode active material loading is about 11 mg cm^{-2}, and the anode active material loading is about 7 mg cm^{-2}. For GP-Ni96 and P-Ni96, the cathode active material loading is about 17 mg cm^{-2}, and the anode active material loading is about 12 mg cm^{-2}. The separator and liquid electrolytes (1 g) were the same as those used in coin-type half-cells. Pouch cells were cycled at 0.1 C three times before cycling at 1 C at 25 °C.

The ASSBs were assembled in a custom-made mold cell inside an Ar-filled glovebox. First, 100 mg Li$_3$InCl$_6$ powder was placed into a poly(ether-ether-ketone) (PEEK) die with a diameter of 10 mm and pressed under 100 MPa, then the cathode mixture was uniformly distributed onto one side of the Li$_3$InCl$_6$ pellet and pressed under 500 MPa. Finally, a piece of Li-In alloy foil was attached on the other side of the Li$_3$InCl$_6$ layer that used Li$_6$PS$_5$Cl as the interlayer to avoid the possible side reactions between Li$_3$InCl$_6$ and the Li-In anode. All the ASSBs were tested under a stack pressure of 100 MPa and at 30 °C. All the electrochemical measurements were carried out using the NEWARE Battery Test System (CT-4008T, Shenzhen, China).

Data availability

All the data generated in this study are provided in the Supplementary Information/Source Data file. Source data are provided with this paper.

References

1. Li, W., Erickson, E. M. & Manthiram, A. High-nickel layered oxide cathodes for lithium-based automotive batteries. *Nat. Energy* **5**, 26–34 (2020).
2. Viswanathan, V. et al. The challenges and opportunities of battery-powered flight. *Nature* **601**, 519–525 (2022).
3. Myung, S.-T. et al. Nickel-rich layered cathode materials for automotive lithium-ion batteries: Achievements and perspectives. *ACS Energy Lett.* **2**, 196–223 (2017).
4. Zhang, R. et al. Compositionally complex doping for zero-strain zero-cobalt layered cathodes. *Nature* **610**, 67–73 (2022).
5. Wang, L., Liu, T., Wu, T. & Lu, J. Strain-retardant coherent perovskite phase stabilized Ni-rich cathode. *Nature* **611**, 61–67 (2022).
6. Liu, T. et al. Understanding Co roles towards developing Co-free Ni-rich cathodes for rechargeable batteries. *Nat. Energy* **6**, 277–286 (2021).
7. Zhou, T. et al. Stabilizing lattice oxygen in slightly Li-enriched nickel oxide cathodes toward high-energy batteries. *Chem* **8**, 2817–2830 (2022).
8. Xu, G.-L. et al. Building ultraconformal protective layers on both secondary and primary particles of layered lithium transition metal oxide cathodes. *Nat. Energy* **4**, 484–494 (2019).
9. Wang, C. et al. Resolving complex intralayer transition motifs in high-Ni-content layered cathode materials for lithium-ion batteries. *Nat. Mater.* **22**, 235–241 (2023).
10. Xu, C. et al. Bulk fatigue induced by surface reconstruction in layered Ni-rich cathodes for Li-ion batteries. *Nat. Mater.* **20**, 84–92 (2021).
11. Qian, G. et al. Structural and chemical evolution in layered oxide cathodes of lithium-ion batteries revealed by synchrotron techniques. *Natl. Sci. Rev.* **9**, nwab146 (2022).
12. Kim, J. et al. Prospect and reality of Ni-rich cathode for commercialization. *Adv. Energy Mater.* **8**, 1702028 (2018).
13. Yang, J., Liang, X., Ryu, H.-H., Yoon, C. S. & Sun, Y.-K. Ni-rich layered cathodes for lithium-ion batteries: From challenges to the future. *Energy Storage Mater.* **63**, 102969 (2023).
14. Ryu, H.-H., Park, K.-J., Yoon, C. S. & Sun, Y.-K. Capacity fading of Ni-rich Li[Ni$_x$Co$_y$Mn$_{1-x-y}$]O$_2$ (0.6 ≤ x ≤ 0.95) cathodes for high-energy-density lithium-ion batteries: Bulk or surface degradation? *Chem. Mat.* **30**, 1155–1163 (2018).
15. Liu, H. et al. Intergranular cracking as a major cause of long-term capacity fading of layered cathodes. *Nano Lett.* **17**, 3452–3457 (2017).
16. Hu, J. et al. Mesoscale-architecture-based crack evolution dictating cycling stability of advanced lithium ion batteries. *Nano Energy* **79**, 105420 (2021).
17. Lim, J.-M. et al. Intrinsic origins of crack generation in Ni-rich LiNi$_{0.8}$Co$_{0.1}$Mn$_{0.1}$O$_2$ layered oxide cathode material. *Sci. Rep.* **7**, 39669 (2017).
18. Woodford, W. H., Carter, W. C. & Chiang, Y.-M. Design criteria for electrochemical shock resistant battery electrodes. *Energy Environ. Sci.* **5**, 8014–8024 (2012).
19. Tsai, P.-C. et al. Single-particle measurements of electrochemical kinetics in NMC and NCA cathodes for Li-ion batteries. *Energy Environ. Sci.* **11**, 860–871 (2018).

20. Cheng, X. et al. Real-time observation of chemomechanical breakdown in a layered nickel-rich oxide cathode realized by in situ scanning electron microscopy. *ACS Energy Lett.* **6**, 1703–1710 (2021).
21. Miller, D. J., Proff, C., Wen, J. G., Abraham, D. P. & Bareño, J. Observation of microstructural evolution in Li battery cathode oxide particles by in situ electron microscopy. *Adv. Energy Mater.* **3**, 1098–1103 (2013).
22. Bi, Y. et al. Reversible planar gliding and microcracking in a single-crystalline Ni-rich cathode. *Science* **370**, 1313–1317 (2020).
23. Qian, G. N. et al. Single-crystal nickel-rich layered-oxide battery cathode materials: synthesis, electrochemistry, and intra-granular fracture. *Energy Storage Mater.* **27**, 140–149 (2020).
24. Yoon, M. et al. Eutectic salt-assisted planetary centrifugal deag-glomeration for single-crystalline cathode synthesis. *Nat. Energy* **8**, 482–491 (2023).
25. Hu, J. et al. Challenges and approaches of single-crystal Ni-rich layered cathodes in lithium batteries. *Natl. Sci. Rev.* **10**, nwad252 (2023).
26. Ryu, H.-H., Lee, S.-B., Yoon, C. S. & Sun, Y.-K. Morphology-dependent battery performance of Ni-rich layered cathodes: single-crystal versus refined polycrystal. *ACS Energy Lett.* **7**, 3072–3079 (2022).
27. Yan, P. et al. Tailoring grain boundary structures and chemistry of Ni-rich layered cathodes for enhanced cycle stability of lithium-ion batteries. *Nat. Energy* **3**, 600–605 (2018).
28. Yoon, M. et al. Reactive boride infusion stabilizes Ni-rich cathodes for lithium-ion batteries. *Nat. Energy* **6**, 362–371 (2021).
29. Ryu, H.-H., Lim, H.-W., Kang, G.-C., Park, N.-Y. & Sun, Y.-K. Long-lasting Ni-rich NCMA cathodes via simultaneous microstructural refinement and surface modification. *ACS Energy Lett.* **8**, 1354–1361 (2023).
30. Kim, U.-H. et al. Heuristic solution for achieving long-term cycle stability for Ni-rich layered cathodes at full depth of discharge. *Nat. Energy* **5**, 860–869 (2020).
31. Park, G.-T. et al. Ultrafine-grained Ni-rich layered cathode for advanced Li-ion batteries. *Energy Environ. Sci.* **14**, 6616–6626 (2021).
32. Sun, H. H. et al. Transition metal-doped Ni-rich layered cathode materials for durable Li-ion batteries. *Nat. Commun.* **12**, 6552 (2021).
33. Liu, T. et al. Rational design of mechanically robust Ni-rich cathode materials via concentration gradient strategy. *Nat. Commun.* **12**, 6024 (2021).
34. Dreyer, S. L. et al. The effect of doping process route on $LiNiO_2$ cathode material properties. *J. Electrochem. Soc.* **170**, 060530 (2023).
35. Weber, D. et al. Tracing low amounts of Mg in the doped cathode active material $LiNiO_2$. *J. Electrochem. Soc.* **169**, 030540 (2022).
36. Gao, Z. et al. Kirkendall effect-induced uniform stress distribution stabilizes nickel-rich layered oxide cathodes. *Nat. Commun.* **15**, 1503 (2024).
37. Li, S. et al. Thermal-healing of lattice defects for high-energy single-crystalline battery cathodes. *Nat. Commun.* **13**, 704 (2022).
38. Mesnier, A. & Manthiram, A. Heuristics for molten-salt synthesis of single-crystalline ultrahigh-nickel layered oxide cathodes. *ACS Appl. Mater. Interf.* **15**, 12895–12907 (2023).
39. Wu, T. et al. Gradient "single-crystal" Li-rich cathode materials for high-stable lithium-ion batteries. *Adv. Funct. Mater.* **33**, 2210154 (2023).
40. Xu, T. et al. Improved rate and cyclic performance of potassium-doped nickel-rich ternary cathode material for lithium-ion batteries. *J. Mater. Sci.* **56**, 2399–2411 (2021).
41. He, T. et al. The effects of alkali metal ions with different ionic radii substituting in Li sites on the electrochemical properties of Ni-Rich cathode materials. *J. Power Sources* **441**, 227195 (2019).
42. Li, Y., Chi, Y., Han, S., Miao, Y. & Chen, L. Investigation on CT characterization of pore structure in nylon-uncured rubber composite from a microscopic view. *Sci. Rep.* **11**, 15682 (2021).
43. Ghadban, M. et al. 3D microscale modeling of NMC cathodes using multi-resolution FIB-SEM tomography. *J. Power Sources* **562**, 232745 (2023).
44. Wang, Y., Li, Z., Li, X., Ma, Z.-F. & Li, L. Catalyzing battery materials research via lab-made, sub-ampere-hour-scale pouch cells, and long-term electrochemical monitoring by a reparable reference electrode. *Adv. Energy Mater.* **14**, 2304512 (2024).
45. Christophersen, J. P. Battery test manual for electric vehicles, revision 3. (2015).
46. Janek, J. & Zeier, W. G. Challenges in speeding up solid-state battery development. *Nat. Energy* **8**, 230–240 (2023).
47. Wang, J., Chen, L., Li, H. & Wu, F. Anode interfacial issues in solid-state Li batteries: mechanistic understanding and mitigating strategies. *Energy Environ. Mater.* **6**, e12613 (2023).
48. Zhou, L. et al. High areal capacity, long cycle life 4 V ceramic all-solid-state Li-ion batteries enabled by chloride solid electrolytes. *Nat. Energy* **7**, 83–93 (2022).
49. Lee, Y.-G. et al. High-energy long-cycling all-solid-state lithium metal batteries enabled by silver–carbon composite anodes. *Nat. Energy* **5**, 299–308 (2020).
50. Hyun, H. et al. Paradoxical role of structural degradation of nickel-rich layered oxides in capacity retention upon storage of lithium-ion batteries. *Energy Environ. Sci.* **16**, 3968–3983 (2023).

Author contributions
Conceptualization: L.S.L., Z.Y.L., and C.H.S. Investigation: Z.Y.L., Y.W., J.W., W.N.W., C.X.W., Y.L.C., C.J.H., K.M., T.G., Y.S.H., Z.H.R., Y.X.Z., X.L., L.W.C., N.L., K.W., and C.H.S. Funding Acquisition: Z.F.M., L.S.L., and L.W.C. Supervision:L.S.L. and C.H.S.

Competing interests
The authors declare no competing interest.

Additional information
Supplementary information The online version contains supplementary material available at https://doi.org/10.1038/s41467-024-54637-9.

Correspondence and requests for materials should be addressed to Chongheng Shen or Linsen Li.

Peer review information *Nature Communications* thanks Panawan Vanaphuti, and the other anonymous reviewers for their contribution to the peer review of this work. A peer review file is available.

Reprints and permissions information is available at http://www.nature.com/reprints

Publisher's note Springer Nature remains neutral with regard to jurisdictional claims in published maps and institutional affiliations.